modelling

MDPI

*Article*

# Surrogate-Assisted Genetic Optimization for Inverse Identification of Hyperelastic Material Parameters from Membrane Inflation Data

**Sabir Hussain [1], Saif Shakeel [1,†], Affan Khan [1,†], Mohammad Rashid Zafar [1,*], Arshad Hussain Khan [1], Thimmappa Shetty Guruprasad [2,*] and Vishwanath Managuli [2]**

[1] Department of Mechanical Engineering, ZHCET, AMU, Aligarh 202002, Uttar Pradesh, India; ah.khan.me@amu.ac.in (A.H.K.)
[2] Manipal Institute of Technology, Manipal Academy of Higher Education, Manipal 576104, Karnataka, India; vishwanath.managuli@manipal.edu
* Correspondence: rashidzafar@zhcet.ac.in (M.R.Z.); guruprasad.shetty@manipal.edu (T.S.G.)
† These authors contributed equally to this work.

**Abstract**

Soft deformable materials such as elastomers, biological tissues, and polymeric membranes are widely used in modern engineering applications including biomechanics, soft robotics, and flexible electronics. Accurate identification of their constitutive parameters is therefore essential for reliable mechanical modeling and design. Membrane inflation or bulge tests are commonly used for this purpose, where material parameters are typically identified from pressure–deflection measurements. However, such measurements generally require optical systems to capture membrane deformation, which increases experimental complexity. In this work, we propose a surrogate-assisted inverse identification framework for determining hyperelastic material parameters using pressure–volume data obtained from membrane inflation tests, thereby eliminating the need for optical deformation measurements. To reduce the computational cost associated with repeated forward simulations, an Artificial Neural Network (ANN) surrogate model is trained using numerically generated pressure–volume data from finite-element simulations. The trained ANN efficiently predicts the pressure response of the membrane for different material parameters and volume influx values. A Genetic Algorithm (GA) is then employed to identify the optimal parameters by minimizing the discrepancy between measured and predicted responses. The proposed GA–ANN framework is demonstrated for the Mooney–Rivlin hyperelastic model and accurately recovers material parameters for both noise-free and noisy datasets, providing a computationally efficient and robust methodology for the characterization of soft membranes.

**Keywords:** surface elasticity; soft solids; inverse problem; genetic algorithm; machine learning



Academic Editor: Wei Gao

Received: 24 June 2026
Revised: 18 July 2026
Accepted: 26 July 2026
Published: 20 August 2026



## 1. Introduction

Highly deformable materials play a prominent role in many emerging technologies and advanced engineering applications. They are widely utilized in fields such as tissue engineering [1], flexible electronics [2], soft robotics [1], soft actuators [3], energy storage devices [4], biomedical devices [5], orthopedic implants [6,7], and electronic packaging [8]. Owing to their extensive and diverse range of applications, significant research efforts have been directed toward achieving a deeper understanding of the mechanical behavior of these materials, particularly under large deformations.

Many of the above-mentioned applications involve thin, soft membranes undergoing large deformations. Accurate characterization of their mechanical behavior is therefore essential for reliable modeling, design, and performance prediction. Over the past decades, numerous experimental and theoretical studies have been conducted to characterize the deformation behavior of soft membranes subjected to large strains. The pioneering experimental investigations of Treloar [9] on the biaxial deformation of rubber established the foundation for constitutive characterization of elastomeric materials and have played a fundamental role in the development and validation of hyperelastic constitutive models. Building upon these foundations, several analytical, numerical, and experimental studies have investigated membrane inflation as an effective approach for characterizing the mechanical response of soft materials. For instance, Luo et al. [10] performed finite-element simulations to compare different equibiaxial testing protocols for rubber-like materials, including uniaxial tension, biaxial tension, and bulge tests. Pelliciari et al. [11] derived analytical expressions describing the pressure–deflection behavior of compressible Mooney–Rivlin membranes under inflation test and validated their results through finite-element simulations and experimental observations. More recently, Di Matteo et al. [12] obtained analytical relations for the pressure–deflection response of incompressible hyperelastic dielectric membranes. These analytical approaches typically rely on simplifying assumptions regarding membrane kinematics.

The inflation of circular membranes has also been widely investigated using numerical and experimental approaches. For example, Chaudhuri and DasGupta [13] examined both the static and dynamic behavior of inflated hyperelastic membranes. Li et al. [14] employed high-speed optical measurement techniques to capture the deformed shapes of membranes during inflation and highlighted the influence of temperature gradients and thermal warpage on parameter identification. Similarly, Patil and DasGupta [15] analyzed the effect of pre-stretch on the inflation behavior of incompressible Mooney–Rivlin membranes, while Verron et al. [16] investigated the dynamic response of hyperelastic spherical and elliptical membranes using finite element methods. More recently, Chen et al. [17] studied the inflation behavior of circular membranes using analytical and numerical methods and identified regions of equibiaxial deformation for different hyperelastic material models.

Among the available constitutive models, relatively simple strain energy functions such as the Mooney-Rivlin model often provide good agreement with experimental observations for membrane deformation problems involving moderate strains [18]. At the same time, ongoing research in soft tissue mechanics has led to the development of increasingly sophisticated constitutive models incorporating features such as anisotropy, fiber reinforcement, viscoelasticity, and damage [19]. For example, Wu et al. [20] proposed a hyperelastic model for human ligaments based on fiber volume fraction, while Anssari-Benam and Saccomandi [21] introduced a hyperelastic formulation to capture the softening behavior of brain tissue. Sirotti et al. [22] designed a deviatoric strain energy function along with volumetric part and calibrated the corresponding parameters using pattern-search optimization applied to experimentally obtained pressure–deflection data.

Accurate identification of material parameters is therefore crucial for reliable constitutive modeling of soft materials. Traditionally, such parameters are obtained from experimental data using inverse identification techniques combined with numerical simulations. For instance, Destrade et al. [23] estimated hyperelastic parameters using uniaxial tension data, while Sheng et al. [24] used bulge test pressure–deflection measurements to calibrate parameters for neo-Hookean and Arruda–Boyce models assuming a spherical cap deformation. However, determination of the central deflection in bulge tests typically requires optical measurement systems [14,22], which may complicate the experimental setup.

Inverse identification of material parameters is fundamentally governed not only by the efficiency of the optimization algorithm but also by the mechanics of the underlying inverse problem. Reliable identification requires that the measured mechanical response exhibits sufficient sensitivity to the unknown parameters so that changes in the parameters produce distinguishable variations in the experimental observables. Parameters with low sensitivity are generally less identifiable, resulting in increased uncertainty and possible non-uniqueness of the inverse solution. Consequently, the selection of the measured response plays an important role in determining the robustness and accuracy of parameter estimation. These issues have been discussed extensively in the material parameter identification literature, particularly in the context of methodical fitting strategies and full-field measurement approaches [23,25]. In the present study, it is shown that the pressure–volume response is considerably more sensitive to the shear modulus than to the normalized Mooney–Rivlin material parameter. As a consequence, the shear modulus can be identified with higher accuracy, whereas the comparatively weaker sensitivity of the normalized Mooney–Rivlin parameter results in larger identification errors in the presence of measurement noise.

Recent studies also highlight the increasing integration of computational modeling and machine learning techniques to improve constitutive model identification and enable data-driven biomechanical simulations [19]. In particular, Artificial Neural Networks have been widely adopted as surrogate models to approximate complex nonlinear relationships between material parameters and mechanical responses, thereby significantly reducing the computational cost associated with repeated numerical simulations. Machine learning-based surrogate models have been successfully applied to accelerate computationally intensive simulations in mechanics, enabling efficient approximation of nonlinear system responses and facilitating rapid evaluation in optimization and inverse analysis problems [26–28]. Such data-driven approaches have demonstrated promising capabilities in accelerating multiscale simulations, solving inverse problems, and enabling efficient parameter identification in nonlinear mechanical systems. Furthermore, recent developments in physics-informed machine learning frameworks, such as Physics-Informed Neural Networks (PINNs), incorporate governing physical laws directly into the training process, allowing neural networks to solve forward and inverse problems governed by partial differential equations while maintaining physical consistency [29,30]. Nevertheless, the application of surrogate-assisted inverse optimization to membrane inflation tests remains relatively limited, particularly for pressure–volume-based characterization where optical deformation measurements are avoided. This represents an important opportunity for developing computationally efficient inverse identification strategies.

Despite the substantial progress achieved in membrane inflation characterization, several challenges remain. First, most existing inverse identification methods rely on pressure–deflection measurements that require optical systems for deformation tracking, thereby increasing experimental complexity. Second, conventional inverse analyses based on finite-element simulations require repeated nonlinear forward computations during optimization, resulting in considerable computational cost. Third, although surrogate modeling techniques have been successfully applied to many inverse mechanics problems, their application to pressure–volume-based membrane inflation for hyperelastic parameter identification has received comparatively little attention. Addressing these limitations forms the primary motivation for the present work.

Motivated by the above limitations, the present work proposes an alternative inverse identification framework based on pressure–volume data obtained from membrane inflation experiments. By replacing the central deflection measurement with the corresponding volume influx, the requirement of optical measurement systems can be eliminated. Instead, the experimental setup can be simplified to include only a pressure sensor and a flow meter for measuring the volume influx of fluid.

To efficiently solve the associated inverse problem, a surrogate modeling strategy based on Artificial Neural Networks (ANNs) is employed. The training dataset is generated using nonlinear finite-element simulations of membrane inflation for a range of Mooney–Rivlin material parameters. The trained ANN serves as a fast surrogate model capable of accurately predicting the pressure–volume response of the membrane. This surrogate model is subsequently coupled with a Genetic Algorithm (GA) to identify the unknown material parameters from the observed pressure–volume data.

The scientific novelty of the present work lies in the integration of three established concepts into a unified inverse characterization framework. Specifically, the proposed methodology combines a pressure–volume-based membrane inflation test, an Artificial Neural Network (ANN) surrogate model, and a Genetic Algorithm (GA) to enable rapid and accurate inverse identification of hyperelastic material parameters without requiring optical deformation measurements. While pressure–volume measurements, surrogate modeling, and evolutionary optimization have each been investigated independently in different contexts, their integration into a single computational framework for pressure–volume-based characterization of hyperelastic membranes has not, to the best of the authors' knowledge, been reported previously.

The remainder of the paper is organized as follows. Section 2 presents the theoretical framework of hyperelasticity, including the relevant deformation and stress measures. Section 3 describes the generation of the training dataset using nonlinear finite-element simulations. Section 4 discusses the architecture and training of the ANN surrogate model. The inverse parameter identification using the Genetic Algorithm is presented in Section 5. Finally, concluding remarks are provided in Section 6.

## 2. Theory of Hyperelasticity

### 2.1. Kinematics

Consider a body occupying a reference configuration $\mathcal{B}_0$ that deforms into another configuration $\mathcal{B}$ at time $t$. An arbitrary point P with position $\boldsymbol{X} \in \mathcal{B}_0$ maps to $\boldsymbol{x} \in \mathcal{B}$ through motion

$$\boldsymbol{x} = \boldsymbol{f}(\boldsymbol{X}, t). \tag{1}$$

The deformed position of a point Q in the close vicinity of point P may be expressed as

$$\boldsymbol{x} + d\boldsymbol{x} = \boldsymbol{f}(\boldsymbol{X} + d\boldsymbol{X}, t). \tag{2}$$

Further, using the Taylor-series expansion,

$$\boldsymbol{x} + d\boldsymbol{x} = \boldsymbol{f}(\boldsymbol{X}, t) + \boldsymbol{F} d\boldsymbol{X}, \tag{3}$$

where $\boldsymbol{F} = \dfrac{\partial \boldsymbol{f}}{\partial \boldsymbol{X}}$ is a measure of deformation and known as the deformation gradient tensor. Similarly, there are other deformations measures such as right and left Cauchy–Green strain tensors defined, respectively, as [31]

$$\begin{aligned} \boldsymbol{C} &= \boldsymbol{F}^T \boldsymbol{F}, \\ \boldsymbol{B} &= \boldsymbol{F} \boldsymbol{F}^T. \end{aligned} \tag{4}$$

*2.2. Stress Measures and Constitutive Relations*

For hyperelastic materials, the stress response is derived from a scalar strain energy density function $\Psi$, which depends on the deformation of the body. The stress tensors can be obtained by differentiating the strain energy function with respect to appropriate deformation measures [31,32].

The first Piola–Kirchhoff stress tensor $\boldsymbol{P}$, which relates forces in the current configuration to areas in the reference configuration, is defined as

$$\boldsymbol{P} = \frac{\partial \Psi}{\partial \boldsymbol{F}}. \tag{5}$$

The second Piola–Kirchhoff stress tensor $\boldsymbol{S}$, which is defined entirely in the reference configuration and is energetically conjugate to the right Cauchy–Green deformation tensor $\boldsymbol{C}$, is given by

$$\boldsymbol{S} = 2\frac{\partial \Psi}{\partial \boldsymbol{C}}. \tag{6}$$

The Cauchy stress tensor $\boldsymbol{\sigma}$, which represents the true physical stress in the current configuration, is related to the strain energy function as

$$\boldsymbol{\sigma} = \frac{1}{J}\boldsymbol{F}\boldsymbol{S}\boldsymbol{F}^T = \frac{2}{J}\boldsymbol{F}\frac{\partial \Psi}{\partial \boldsymbol{C}}\boldsymbol{F}^T, \tag{7}$$

where $J = \det(\boldsymbol{F})$ represents the ratio of deformed and reference infinitesimal volume elements.

In case of isotropic materials, the strain energy density may be written as $\Psi = \Psi(I_1, I_2, I_3)$ with $I_1$, $I_2$ and $I_3$ being invariants of $\boldsymbol{C}$. Further, for incompressible isotropic material, the energy density function becomes $\Psi = \Psi(I_1, I_2)$ as $I_3 = 1$. In such cases, the Cauchy stress tensor additionally includes a hydrostatic pressure term to enforce the incompressibility constraint, i.e.,

$$\boldsymbol{\sigma} = -p\boldsymbol{I} + \frac{2}{J}\boldsymbol{F}\frac{\partial \Psi}{\partial \boldsymbol{C}}\boldsymbol{F}^T, \tag{8}$$

where $p$ is a Lagrange multiplier associated with the incompressibility constraint. The material model used in the current study was a Mooney–Rivlin model with functional form

$$\Psi = C_1(I_1 - 3) + C_2(I_2 - 3), \tag{9}$$

where $C_1$ and $C_2$ are material constants. Among the available hyperelastic constitutive models, the two-parameter Mooney–Rivlin model was selected because it provides a simple yet sufficiently accurate representation of the large deformation response of many incompressible isotropic rubber-like materials. Furthermore, it represents a generalization of the neo-Hookean model while requiring only two material parameters, making it well suited for demonstrating the proposed inverse identification framework.

## 3. Dataset Generation: Finite Element Method

Nonlinear finite-element (FE) simulations were performed in order to generate dataset for training the ANN. A soft circular membrane of radius $R$ and thickness $t$ was fixed over a hollow cylinder with one end closed (as shown in Figure 1). The membrane was inflated by applying pressure beneath the membrane, and its response was simulated using commercial FE software Abaqus 2023. However, as the pressure response is non-monotonic [17], the pressure control simulation can only capture the response up to the monotonicity limit using the Newton–Raphson Method. Hence, we performed the analysis using the volume influx in the hollow cavity beneath the membrane. Axisymmetric analysis was performed by exploiting the rotational symmetry of the problem. A fixed boundary condition in $r$-direction was applied to the axis of rotation while the lateral surface of the membrane was completely fixed.

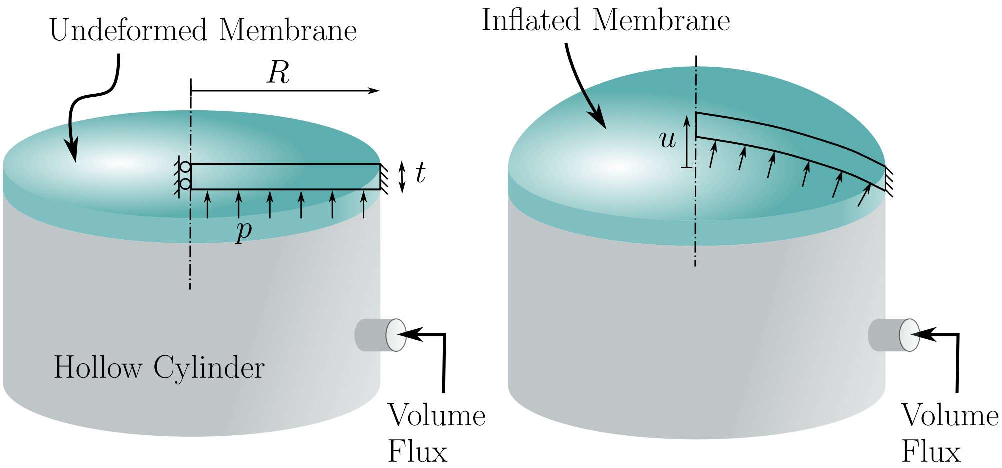


**Figure 1.** Bulge test setup: on the (**left**), an undeformed circular membrane of radius $R$ and thickness $t$ is fixed over a rigid hollow cylinder closed from the bottom; on the (**right**), inflated membrane obtained by prescribing the volume influx into the fluid-filled cavity beneath the membrane.

The membrane was discretized into 4-noded quadrilateral axisymmetric hybrid elements. The hybrid formulation was used to incorporate the incompressibility of the material using hydrostatic pressure as an additional degree of freedom in the element. In order to model the volume influx in the hollow cylindrical cavity, fluid cavity elements of Abaqus were used, which are based on a volume constraint formulation. The Mooney–Rivlin material model was used to run the finite-element simulation, along with a special choice of parameter ($C_2 = 0$) giving a neo-Hookean response.

### 3.1. Validation of Finite-Element Results

The finite-element (FE) results were validated against published results available in the literature. The geometrical and material parameters used in the validation study are listed in Table 1. Figure 2a shows the variation in pressure with the vertical displacement of the membrane center, demonstrating good agreement with the results of Chen et al. [17]. In addition, the non-dimensional pressure–volume response was compared with the results reported by Selvadurai [33], as shown in Figure 2b, where a close agreement is observed. Note that pressure was non-dimensionalized by $\mu = 2(C_1 + C_2)$ for the Mooney–Rivlin material.

**Table 1.** Geometry and material details for validation of FE results.

| Literature | $t$ (mm) | $R$ (mm) | Materials Parameters (MPa) |
|---|---|---|---|
| [17] | 1 | 60 | neo-Hookean ($\mu = 0.4$)<br>Mooney–Rivlin ($C_1 = 0.162$, $C_2 = 0.0059$) |
| [33] | 0.8 | 73 | Mooney–Rivlin ($C_1 = 0.242$, $C_2 = 0.142$) |

https://doi.org/10.3390/modelling7040175

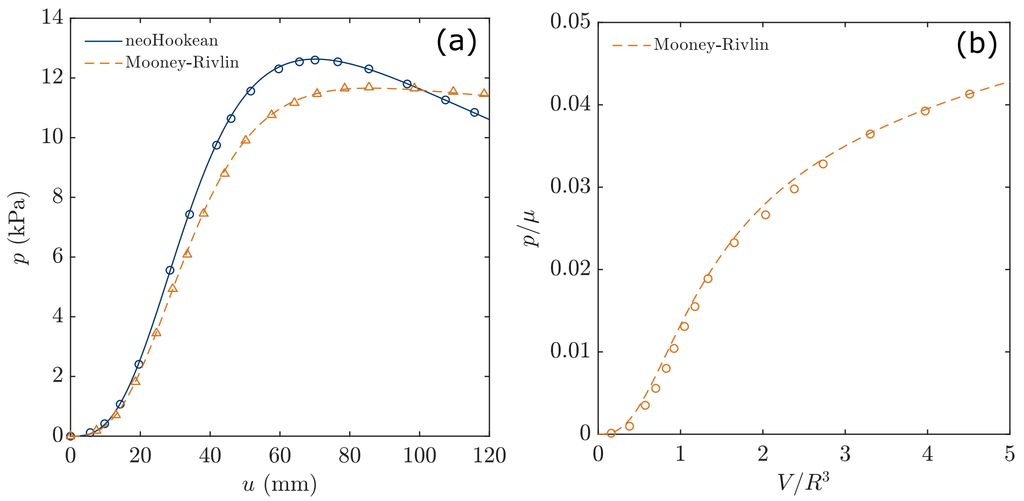


**Figure 2.** Comparison of the present FE results (lines) for membrane inflation with literature data (markers) (**a**) [17] for pressure–deflection and (**b**) [33] for non-dimensional pressure–volume responses.

### 3.2. Scale Invariance of the Non-Dimensional Response

In order to establish a consistent non-dimensional framework, different combinations of material parameters, namely, the shear modulus $\mu$ and the Mooney–Rivlin parameter $C_1$, were considered. While maintaining a constant thickness-to-radius ratio of $t/R = 1/50$, two different geometric scales were analyzed to verify the scale invariance of the formulation. The complete set of material and geometric parameters used in the study is summarized in Table 2.

**Table 2.** Geometry and material parameters for non-dimensional study.

| $t/R$ | $\overline{C}_1 = C_1/\mu$ | $C_1$ | mu | $t$ | $R$ |
|---|---|---|---|---|---|
| 1/50 | 0.5 | 0.5 | 1 | 1 | 50 |
| | | 5 | 10 | 1 | 50 |
| | | 50 | 100 | 1 | 50 |
| | | 0.5 | 1 | 10 | 500 |
| | 0.4 | 0.5 | 1 | 1 | 50 |
| | | 5 | 10 | 1 | 50 |
| | | 50 | 100 | 1 | 50 |
| | | 0.5 | 1 | 10 | 500 |
| | 0.1 | 0.5 | 1 | 1 | 50 |
| | | 5 | 10 | 1 | 50 |
| | | 50 | 100 | 1 | 50 |
| | | 0.5 | 1 | 10 | 500 |

The variation in pressure, non-dimensionalized by the shear modulus $\mu$, is plotted against the vertical displacement at the center, non-dimensionalized by the radius $R$, as shown in Figure 3a. The results demonstrate that when expressed in non-dimensional form, the pressure–displacement response becomes independent of the absolute values of the material and geometric parameters, provided the ratios $C_1/\mu$ and $t/R$ are kept constant. This observation provides the foundation for formulating the problem in a non-dimensional framework. Such a formulation allows the membrane response to be represented in a generalized manner, independent of the absolute values of material and geometric parameters. Therefore, the subsequent analysis was carried out using appropriate non-dimensional variables.

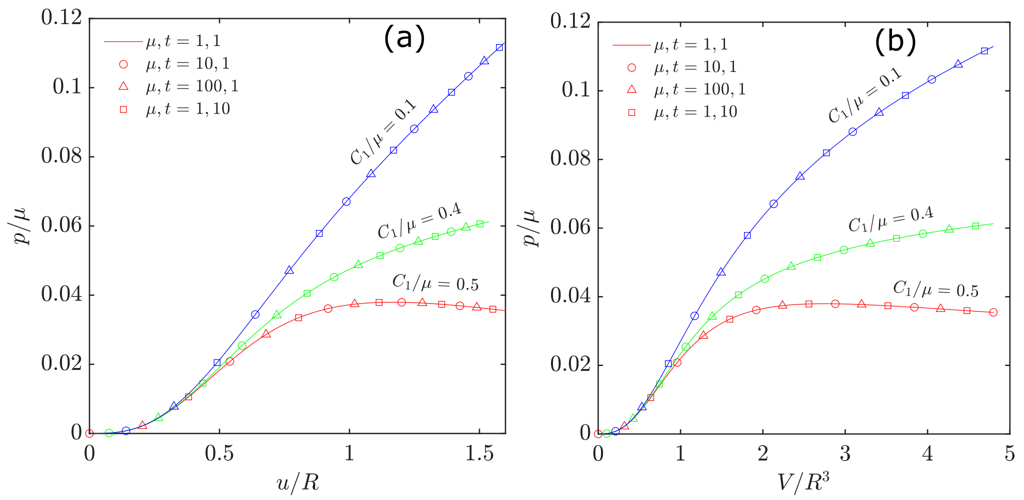


**Figure 3.** Variation of non-dimensionalized pressure with (**a**) normalized displacement at the center of the membrane and (**b**) normalized volume influx to inflate the membrane for different material parameters and geometries.

Similarly, the pressure–volume relationship, shown in Figure 3b, further confirms the scale invariance of the problem. It is observed that for fixed values of the ratios $C_1/\mu$ and $t/R$, the response of the membrane remains unchanged irrespective of the individual values of $\mu$ and $R$. This demonstrates that the mechanical behavior of the membrane is governed primarily by the non-dimensional parameters rather than their dimensional counterparts. Consequently, the non-dimensional framework provides a generalized representation of the system behavior, enabling the results to be applied across different material stiffnesses and geometric scales.

### 3.3. Material Parameter Space for Data Generation

Once the non-dimensionalized formulation was established, we generated an extensive dataset for pressure and volume influx for 33 uniformly distributed material parameter values, i.e., $\overline{C}_1 = C_1/\mu$ in the range (0.1–0.5). Although the theoretically admissible range of $\overline{C}_1$ is (0–0.5), values less than 0.1 indicate that the contribution of $\overline{C}_2$ (i.e., $C_2/\mu$) to the strain–energy function is significantly larger than that of $\overline{C}_1$. Such parameter combinations are less commonly reported. Therefore, a lower bound 0.1 was selected to focus on a practically relevant range. The aspect ratio of the membrane was chosen as $\overline{t} = t/R = 1/50$. For each material parameter value, 100 data points for pressure $\overline{p} = p/\mu$ were generated using FE simulations for the given volume influx $\overline{V} = V/R^3$ of fluid beneath the membrane. A snippet of dataset generated is shown in Table 3.

**Table 3.** A snippet of dataset generated through FE simulation for training of the ANN.

| $\overline{C}_1$ | $\overline{V}$ | $\overline{p}$ |
|---|---|---|
| 0.1 | 0 | 0 |
| 0.1 | 1.824 | 0.05825 |
| 0.1125 | 1.296 | 0.03927 |
| 0.125 | 1.344 | 0.04084 |
| 0.15 | 2.64 | 0.07509 |
| 0.1625 | 2.352 | 0.06827 |
| 0.1625 | 2.4 | 0.06928 |
| 0.2 | 2.88 | 0.07475 |

The pressure–displacement and pressure–volume data are plotted for an arbitrary choice of material parameter $\overline{C}_1$ in Figure 4. We chose three levels of mesh refinement (5, 10 and 20 elements across the thickness) in order to ensure mesh convergence. It is clear from Figure 4 that for two representative material parameter values, the response for all three mesh levels are in good agreement. For the rest of the simulations, we chose the intermediate level of mesh size, i.e., 10 elements across the thickness, as shown in Figure 5a. The deformed shapes for the same representative cases are shown in Figure 5b with contour colors representing vertical displacement.

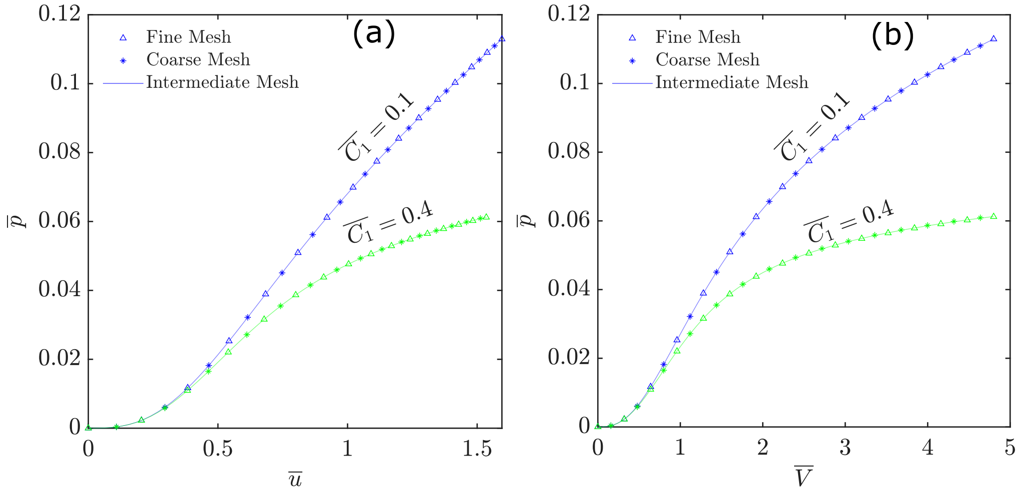


**Figure 4.** Effect of mesh refinement over (**a**) pressure–displacement and (**b**) pressure–volume response of the membrane for two representative cases of material parameters.

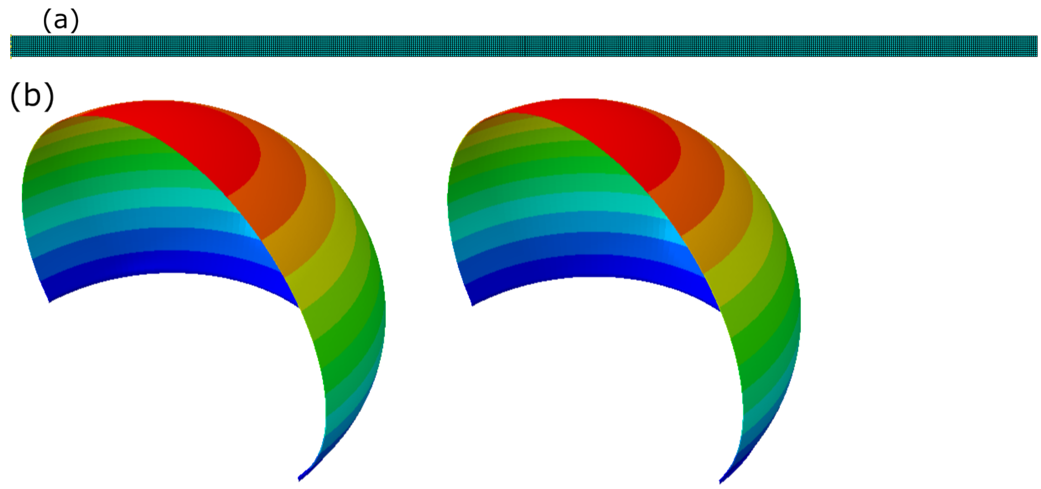


**Figure 5.** (**a**) Axisymmetric structured mesh with 10 elements across the thickness, (**b**) full sectional deformed shapes of membrane with material parameter $\overline{C}_1 = 0.4$ on the (**left**) and $\overline{C}_1 = 0.1$ on the (**right**) for volume influx $\overline{V} = 4.8$. The contours are presented only to qualitatively illustrate the deformed shape of the membrane.

## 4. Training of ANN

An ANN was trained to serve as a surrogate model for the pressure response of the membrane. Non-dimensionalized Mooney–Rivlin parameter $\overline{C}_1$ and volume influx $\overline{V}$ were selected as features, and pressure response was the target. The architecture of the network was selected with two hidden layers, each with 20 neurons. The activation function used in the hidden layers was 'tansig', while a linear activation function was selected for the output layer (Figure 6). This architecture was chosen by trial and error. The complete dataset was randomly divided into training (70%), validation (15%) and testing (15%) subsets. The stopping criteria for the training were (i) a maximum number of epochs of 20,000, (ii) a

Mean Square Error (MSE) becoming zero, (iii) a gradient of MSE below $1 \times 10^{-12}$ or (iv) six consecutive epochs without improvement in the validation error.

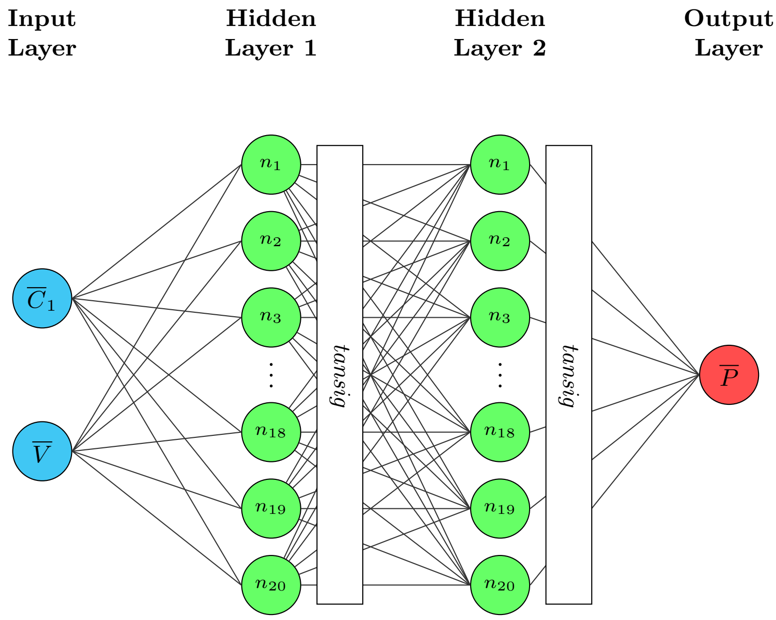


**Figure 6.** ANN with two hidden layers.

The performance metrics, including MAE, MSE, RMSE, and $R^2$, are summarized in Table 4. The very small values of MAE, MSE, and RMSE for the training, validation, and testing datasets indicate that the ANN is able to predict the target values with high accuracy. Moreover, the errors remain of the same order of magnitude across all three datasets, which suggests that the network has learned the underlying relationship effectively without overfitting the training data. The coefficient of determination ($R^2$) is equal to unity for all datasets, indicating an excellent agreement between the predicted and FE-generated pressure values. These results demonstrate that the trained ANN provides accurate and consistent predictions.

**Table 4.** Performance metrics of trained ANN on training, validation and test datasets.

| | MAE | MSE | RMSE | $R^2$ |
|---|---|---|---|---|
| Training | $5.14 \times 10^{-9}$ | $5.54 \times 10^{-17}$ | $7.44 \times 10^{-9}$ | 1 |
| Validation | $6.72 \times 10^{-9}$ | $1.91 \times 10^{-16}$ | $1.38 \times 10^{-8}$ | 1 |
| Testing | $7.88 \times 10^{-9}$ | $4.61 \times 10^{-16}$ | $2.15 \times 10^{-8}$ | 1 |

The very high prediction accuracy of the ANN surrogate, reflected by $R^2$ values very close to unity for the training, validation, and testing datasets should be interpreted in the context of the dataset used in this study. The pressure–volume data were generated through deterministic FE simulations under idealized conditions and are therefore free from experimental measurement errors and stochastic variability. Consequently, the dataset exhibits a smooth and consistent nonlinear relationship between the input variables and the target pressure response, enabling the ANN to learn this mapping with exceptionally high accuracy. It is acknowledged that lower prediction accuracy may be expected when the surrogate model is trained or evaluated using experimental data containing measurement noise and other uncertainties.

Additionally, the predicted values of pressure are plotted against the target values in Figure 7a–c for training, validation and testing datasets. The points are almost exactly lying at the 45° reference line showing excellent agreement between the predicted and target values for all the data subsets. The convergence behavior is also shown in Figure 7d for all the data subsets. It shows smooth learning characteristics for training, validation and testing losses. The converged graph for training represents the completion of training while the convergence of validation loss points corresponds to the absence of overfitting.

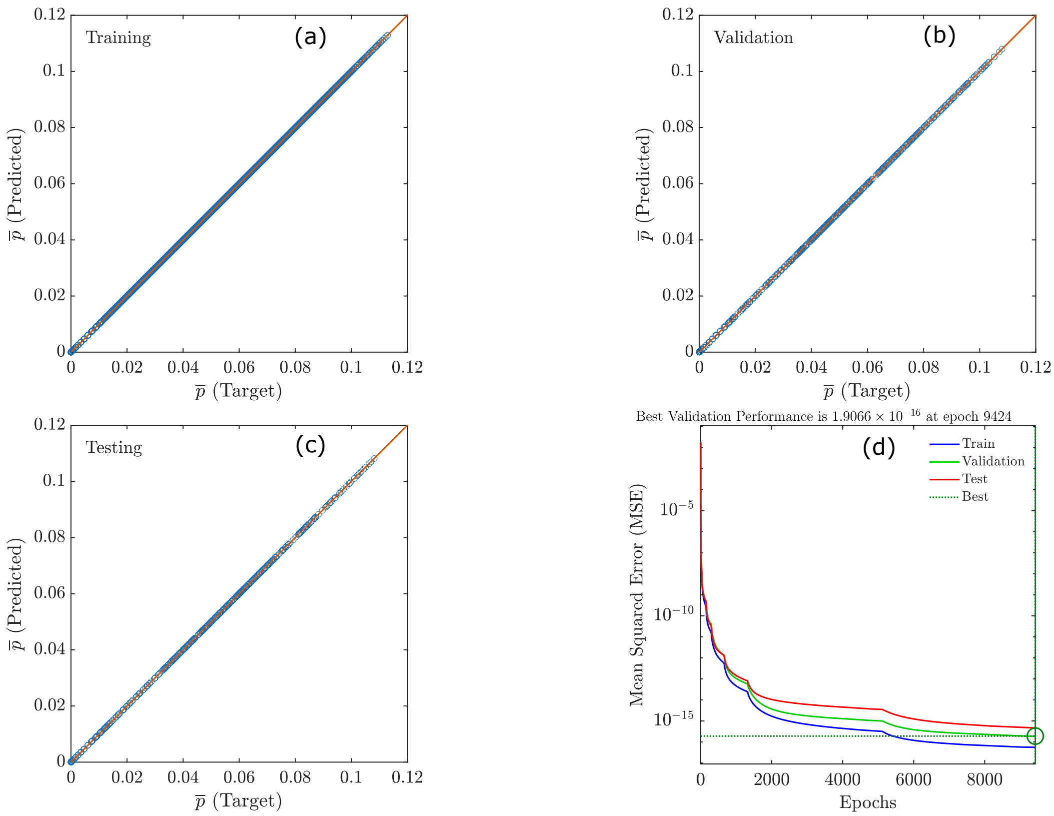


**Figure 7.** Regression plots for (**a**) training, (**b**) validation and (**c**) testing datasets with circles representing the data while red lines show the ideal 45° line for perfect prediction. (**d**) Convergence plot for all the datasets.

To further justify the selection of the ANN surrogate model, a Gaussian Process Regression (GPR) model was also developed and evaluated as an alternative probabilistic surrogate modeling approach capable of capturing nonlinear relationships. The GPR model was trained using 70% of the same dataset, while the remaining 30% was reserved for testing. For the test dataset, the GPR model yielded an RMSE value of $1.23 \times 10^{-4}$, which is four orders of magnitude higher than that obtained using the ANN model (Table 4). Nevertheless, the coefficient of determination ($R^2$) for the GPR model was found to be close to unity. These results indicate that although GPR provides a good overall fit, the ANN model offers substantially lower prediction error and was therefore retained as the surrogate model in the present study.

## 5. Genetic Algorithm for Inverse Optimization

The objective of the present study was to identify the material parameters, $\mu = 2(C_1 + C_2)$ and $C_1$, using the experimentally obtained pressure–volume data. A Genetic Algorithm (GA) was implemented to solve the inverse problem posed as an optimization task. While optimization calls the solution of forward problems repetitively, an ANN surrogate model was used for this purpose instead of opting for the FE-based solution method. It is important to note that in the current study, the time taken by the trained ANN model to predict the pressure for 100 discrete volumes was around 0.004 s while for the same task, it took around 17 min using the FE method on a workstation equipped with an

Intel Xeon Silver 4316 processor (2.30 GHz, 80 logical cores), 128 GB of RAM. Thus, the ANN surrogate was $>10^5$ times faster than the FE-based forward solver. The flow chart in Figure 8 shows the workflow of the optimization process. It should be noted that a practical implementation of pressure–volume inflation tests may involve additional sources of experimental uncertainty, such as sensor calibration, dead volume, system compliance, leakage, and thermal effects, which are beyond the scope of the present numerical study.

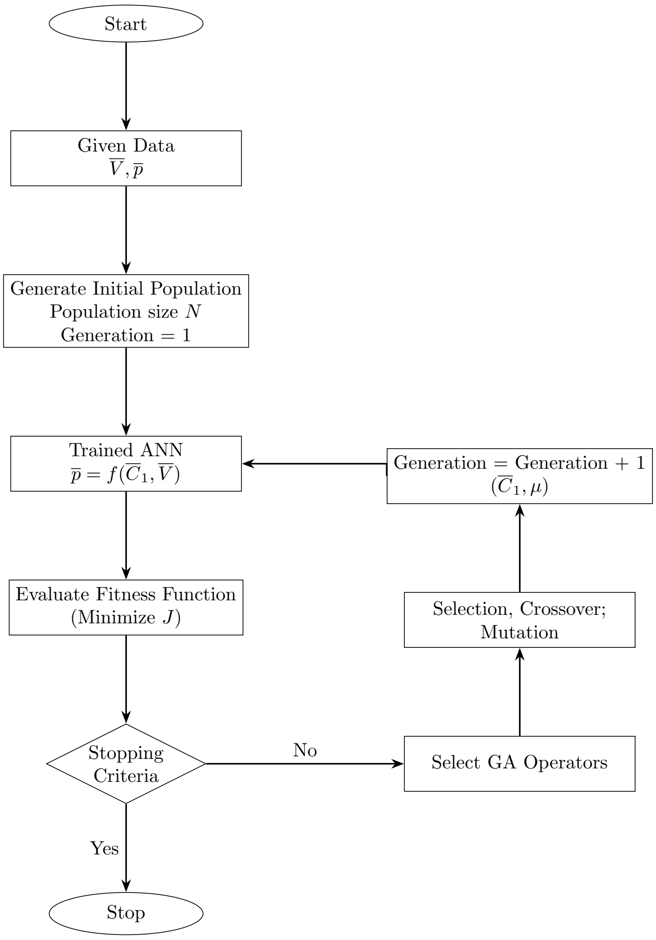


**Figure 8.** Workflow of GA–ANN surrogate optimization process.

Although the present inverse identification problem involves only two material parameters, the pressure–volume response of the inflated hyperelastic membrane is highly nonlinear, which may result in a complex optimization landscape with multiple local minima. Therefore, a GA was selected because it provides a robust global search strategy over the prescribed parameter space, does not require gradient information, and is comparatively less sensitive to the choice of initial guesses. These features make GAs suitable for the present inverse problem. It is acknowledged that deterministic optimization methods, such as gradient-based or pattern-search algorithms, may also be effective for problems with a limited number of parameters. A direct comparative study between GAs and deterministic methods is beyond the scope of the present work but represents an important direction for future research.

Firstly, we implemented the GA to predict the parameters using the response data generated through FE simulations. The responses used for training the ANN as well as responses unseen by the ANN were used to demonstrate the effectiveness of the proposed method. Subsequently, we assessed the performance of the GA–ANN surrogate approach for the prediction of parameters using the same data with added noise mimicking the experimental uncertainty.

*5.1. Objective Function for Parameter Identification*

The parameter identification problem was posed as a minimization of a scalar fitness function. The fitness function was defined as the Mean Squared Error (MSE) in the predicted and target pressure responses for a number of discrete volumes, i.e.,

$$\text{Minimize } J(\mu_s, \overline{C}_1)$$
$$J(\mu, \overline{C}_1) = \frac{1}{n}\sum_{i=1}^{n}\left[\frac{p_i^{\text{tar}}(\overline{V}_i)}{A} - \mu_s\, \overline{p}_i(\overline{C}_1, \overline{V}_i)\right]^2, \tag{10}$$

where $p_i^{\text{tar}}(\overline{V}_i)$ represents the target pressure for the $i$th normalized volume $\overline{V}_i$ while $\overline{p}_i(\overline{C}_1, \overline{V}_i)$ stands for the ANN-predicted normalized pressure and is dependent on non-dimensionalized Mooney–Rivlin parameter $\overline{C}_1$. In the above expression,

$$A = 10 \max_{1 \le i \le n}\left(p_i^{\text{tar}}\right) \tag{11}$$

is a scaling factor, introduced to improve numerical conditioning and enhance the convergence characteristics of the optimization algorithm. Upon convergence of the GA, the dimensional shear modulus is recovered from the optimized value of $\mu_s$ using the relation $\mu = \mu_s\, A$.

*5.2. Genetic Algorithm Implementation Details*

The Genetic Algorithm was implemented to minimize the objective function defined in Equation (10) and identify the unknown material parameters within the prescribed search space. The optimization was performed using the trained ANN surrogate model for evaluating the pressure response corresponding to each candidate solution. This subsection describes the design variables, parameter bounds, and the specific GA settings used in the present study.

5.2.1. Design Variables and Search Space

The material parameters to be identified were the shear modulus $\mu$ and the Mooney–Rivlin parameter $C_1$. However, since the ANN surrogate model was trained using non-dimensional variables, the optimization was performed to evaluate $\mu_s$ and the normalized parameter $\overline{C}_1$. The other Mooney–Rivlin parameter was obtained using $\overline{C}_2 = 0.5 - \overline{C}_1$. The search range for design variable $\overline{C}_1$ was selected to be consistent with the parameter space used for dataset generation, i.e., $0.1 \le \overline{C}_1 \le 0.5$. This range ensured that the ANN surrogate model operated within the domain over which it had been trained, thereby maintaining prediction accuracy and avoiding extrapolation errors. On the contrary, the search range for $\mu$ had no such limitation, as the surrogate network was completely non-dimensionalized and independent of $\mu$. However, we selected the range of scaled shear modulus to be $0.1 \le \mu_s \le 1000$.

5.2.2. Genetic Algorithm Parameters and Optimization Procedure

A GA performs a global search within the prescribed parameter bounds by evolving a population of candidate solutions over successive generations using biologically inspired operators such as selection, crossover, and mutation.

Each individual in the population represented a candidate solution defined by the pair of design variables $(\mu_s, \overline{C}_1)$. The initial population was generated randomly within the specified bounds to ensure uniform coverage of the search space. The fitness of each individual was evaluated using the objective function, which measured the discrepancy between the target pressure response and the ANN-predicted pressure response corresponding to the candidate material parameters.

The Genetic Algorithm was implemented using MATLAB R2025a. The key GA parameters used in the present study are summarized below:

- Population size: 100.
- Maximum number of generations: 500.
- Elite count: $\lceil 0.05 \times \texttt{Population Size} \rceil$.
- Crossover fraction: 0.8.
- Stopping criteria:
  - Maximum number of generations (500) reached;
  - Stall generations limit reached (no improvement in fitness value over 50 generations);
  - Function tolerance $10^{-12}$ satisfied.

The elite preservation strategy was used to ensure that the best-performing individuals were carried forward to subsequent generations without modification, thereby improving convergence stability. The crossover operator generates new candidate solutions by combining information from selected parent individuals, promoting efficient exploration of the search space. The mutation operator introduces controlled random variations, which helps maintain diversity in the population and prevents premature convergence to local minima.

For each candidate solution generated during the optimization process, the normalized pressure response corresponding to the prescribed volume influx values was predicted using the trained ANN surrogate model. The dimensional pressure was then obtained by scaling the normalized pressure using the shear modulus $\mu$, and the fitness value was computed using Equation (10). Since the ANN surrogate provides rapid predictions, the fitness evaluation can be performed with significantly reduced computational cost compared to direct finite-element simulations.

The optimization process proceeded iteratively, with the population evolving toward improved solutions in successive generations. At each generation, individuals with better fitness values had a higher probability of being selected for reproduction, thereby guiding the search toward the optimal material parameters. The optimization terminated when one of the stopping criteria was satisfied, and the individual with the minimum objective function value was selected as the identified solution.

### *5.3. Parameter Identification Results*

The GA–ANN based optimization framework was employed to identify the Mooney–Rivlin material parameters, the shear modulus $\mu$ and the normalized parameter $\overline{C}_1$, using artificially generated pressure–volume data. Since the forward surrogate model was trained using non-dimensional variables, the volume was non-dimensionalized with respect to $R^3$. However, as the shear modulus $\mu$ was itself an unknown parameter, the pressure could not be non-dimensionalized and therefore appeared in dimensional form in the objective function.

Table 5 presents the actual and identified values of the material parameters for different pressure–volume datasets covering a wide range of shear modulus values. Out of these, the last four rows represent the prediction for material parameters completely unseen by the ANN. The results demonstrate excellent agreement between predicted and actual values of both the parameters for all cases.

Overall, the results indicate that the proposed GA–ANN framework is capable of accurately identifying both material parameters over a broad range of $\mu$ values. Nevertheless, the prediction accuracy remains well within acceptable limits, demonstrating the robustness and effectiveness of the proposed inverse identification approach.

**Table 5.** Actual and predicted values of Mooney–Rivlin parameters with numerically generated pressure–volume data.

| Sr. No. | $\mu$ (Actual) | $\mu$ (Predicted) | % Error | $\overline{C}_1$ (Actual) | $\overline{C}_1$ (Predicted) | % Error |
|---|---|---|---|---|---|---|
| 1 | 1 | 1.00004 | 0.004 | 0.1 | 0.10004 | 0.036 |
| 2 | 1 | 1.00001 | 0.001 | 0.2 | 0.20001 | 0.005 |
| 3 | 1 | 1.00001 | 0.001 | 0.3 | 0.3 | 0.002 |
| 4 | 1 | 0.99999 | 0.001 | 0.4 | 0.4 | 0.001 |
| 5 | 1 | 0.99999 | 0.001 | 0.5 | 0.5 | 0 |
| 6 | 10 | 10.0006 | 0.006 | 0.1 | 0.10005 | 0.051 |
| 7 | 10 | 10.0001 | 0.001 | 0.2 | 0.20001 | 0.005 |
| 8 | 10 | 10.0001 | 0.001 | 0.3 | 0.3 | 0.001 |
| 9 | 10 | 10.0001 | 0.001 | 0.4 | 0.4 | 0.001 |
| 10 | 10 | 9.9999 | 0.001 | 0.5 | 0.5 | 0 |
| 11 | 100 | 100.004 | 0.004 | 0.1 | 0.10004 | 0.04 |
| 12 | 100 | 100.003 | 0.003 | 0.2 | 0.20002 | 0.012 |
| 13 | 100 | 100.001 | 0.001 | 0.3 | 0.30001 | 0.002 |
| 14 | 100 | 99.999 | 0.001 | 0.4 | 0.4 | 0.001 |
| 15 | 100 | 100 | 0 | 0.5 | 0.5 | 0 |
| 16 | 1000 | 1000.04 | 0.004 | 0.1 | 0.10004 | 0.037 |
| 17 | 1000 | 1000.08 | 0.008 | 0.2 | 0.20006 | 0.029 |
| 18 | 1000 | 1000.01 | 0.001 | 0.3 | 0.30001 | 0.002 |
| 19 | 1000 | 1000.01 | 0.001 | 0.4 | 0.4 | 0 |
| 20 | 1000 | 999.99 | 0.001 | 0.5 | 0.5 | 0 |
| 21 | 1 | 1 | 0 | 0.135 | 0.135 | 0.002 |
| 22 | 10 | 10.0003 | 0.003 | 0.165 | 0.16502 | 0.012 |
| 23 | 100 | 99.999 | 0.001 | 0.442 | 0.442 | 0.001 |
| 24 | 1000 | 999.98 | 0.002 | 0.49 | 0.48999 | 0.001 |

### *5.4. Robustness Under Noisy Response*

The robustness of the proposed optimization framework was also evaluated in the presence of noise in the data. To simulate experimental uncertainty, a uniformly distributed random noise of 5% was added to the numerically generated pressure corresponding to the prescribed volume values. The noisy pressure was expressed as

$$p(V) = p(V) + p(V)\,\mathcal{U}(-0.05, 0.05), \tag{12}$$

where $\mathcal{U}(-0.05, 0.05)$ represents a uniformly distributed random variable in the range $-0.05$ to 0.05. This procedure mimics realistic measurement noise encountered in experimental pressure–volume data. A uniform distribution was adopted because it provides a simple non-parametric model in which all perturbations within the specified uncertainty band are considered equally probable. We acknowledge that pressure-sensor errors are often well approximated by Gaussian noise; therefore, the present noise model should be regarded as a generalized robustness test rather than a sensor-specific statistical representation. Future work may incorporate Gaussian or experimentally characterized noise distributions to further evaluate the robustness of the proposed framework.

The actual and predicted values of the material parameters obtained from the noisy data are reported in Table 6. It is observed that the maximum error in the prediction of the shear modulus $\mu$ is approximately 2.5%, indicating that the proposed framework remains stable and accurate even in the presence of significant noise.

**Table 6.** Actual and predicted values of Mooney–Rivlin parameters for noisy pressure–volume data.

| Sr. No. | $\mu$ (Actual) | $\mu$ (Predicted) | % Error | $\overline{C}_1$ (Actual) | $\overline{C}_1$ (Predicted) | % Error |
|---|---|---|---|---|---|---|
| 1 | 1 | 0.99963 | 0.037 | 0.1 | 0.10003 | 0.028 |
| 2 | 1 | 0.99421 | 0.579 | 0.2 | 0.19139 | 4.307 |
| 3 | 1 | 1.00257 | 0.257 | 0.3 | 0.29954 | 0.155 |
| 4 | 1 | 1.01001 | 1.001 | 0.4 | 0.4051 | 1.274 |
| 5 | 1 | 1.00109 | 0.109 | 0.5 | 0.5 | 0 |
| 6 | 10 | 10.0641 | 0.641 | 0.1 | 0.1 | 0 |
| 7 | 10 | 9.9456 | 0.544 | 0.2 | 0.19457 | 2.717 |
| 8 | 10 | 9.903 | 0.97 | 0.3 | 0.29315 | 2.284 |
| 9 | 10 | 9.8342 | 1.658 | 0.4 | 0.39453 | 1.368 |
| 10 | 10 | 9.983 | 0.17 | 0.5 | 0.49995 | 0.009 |
| 11 | 100 | 101.256 | 1.256 | 0.1 | 0.11083 | 10.835 |
| 12 | 100 | 98.969 | 1.031 | 0.2 | 0.18689 | 6.553 |
| 13 | 100 | 101.617 | 1.617 | 0.3 | 0.30743 | 2.475 |
| 14 | 100 | 99.269 | 0.731 | 0.4 | 0.39544 | 1.14 |
| 15 | 100 | 100.359 | 0.359 | 0.5 | 0.5 | 0 |
| 16 | 1000 | 1003.72 | 0.372 | 0.1 | 0.10408 | 4.081 |
| 17 | 1000 | 1007.02 | 0.702 | 0.2 | 0.20531 | 2.656 |
| 18 | 1000 | 994.76 | 0.524 | 0.3 | 0.29483 | 1.724 |
| 19 | 1000 | 975.89 | 2.411 | 0.4 | 0.3884 | 2.901 |
| 20 | 1000 | 1002.28 | 0.228 | 0.5 | 0.5 | 0 |
| 21 | 1 | 0.97993 | 2.007 | 0.135 | 0.11978 | 11.277 |
| 22 | 10 | 9.8018 | 1.982 | 0.165 | 0.15007 | 9.046 |
| 23 | 100 | 100.075 | 0.075 | 0.442 | 0.44208 | 0.019 |
| 24 | 1000 | 1007.06 | 0.706 | 0.49 | 0.49073 | 0.149 |

In contrast, relatively higher errors are observed in the prediction of $\overline{C}_1$ for certain cases. This difference can be explained from a parameter sensitivity and identifiability perspective. The pressure response exhibits higher sensitivity to variations in the shear modulus $\mu$ compared to $C_1$, i.e., $\partial p/\partial \mu > \partial p/\partial C_1$ over the considered deformation range. As a result, changes in $\mu$ produce more pronounced variations in the pressure response, making it easier to identify accurately even when noise is present. On the other hand, the comparatively weaker influence of $C_1$ on the pressure response reduces its identifiability, making its estimation more sensitive to measurement noise.

From an inverse-problem standpoint, parameters with lower sensitivity contribute less to the gradient of the objective function, resulting in a flatter optimization landscape in those directions. Consequently, small perturbations in the response data can produce relatively larger variations in the identified values of such parameters. Despite this inherent limitation, the prediction errors remain within acceptable bounds, and the overall results demonstrate that the proposed optimization framework is robust and capable of reliably identifying material parameters from noisy datasets.

### *5.5. Repeatability and Statistical Assessment of the Identified Parameters*

To assess the repeatability of the proposed inverse identification strategy, the GA–ANN optimization procedure was performed independently $n = 30$ times for each of the two cases with the highest error in Table 6, i.e., $(\mu,\ \overline{C}_1) = (1,\ 0.135)$ and $(100,\ 0.1)$. Owing to the stochastic nature of the Genetic Algorithm, each run was initialized with a different random population. In addition, for every run, a newly generated random noise realization was superimposed on the synthetic pressure response. This approach enabled the evaluation of the consistency of the identified parameters under repeated executions of the optimization routine.

Let $\hat{\theta}_i$ denote the value of a parameter ($\mu$ or $\overline{C}_1$) obtained from the $i$th run. The sample mean of the identified parameter is defined as

$$\overline{\theta} = \frac{1}{n}\sum_{i=1}^{n}\hat{\theta}_i,$$

and the corresponding sample standard deviation is given by

$$s = \sqrt{\frac{1}{n-1}\sum_{i=1}^{n}\left(\hat{\theta}_i - \overline{\theta}\right)^2}.$$

Since the population variance is not known a priori, the confidence interval for the mean estimate was constructed using the Student's $t$-distribution with $(n-1)$ degrees of freedom:

$$CI_{1-\alpha} = \overline{\theta} \pm \frac{s}{\sqrt{n}}\, t_{(\alpha/2,n-1)}.$$

The mean values, standard deviations, and corresponding 95% confidence bounds obtained from 30 independent runs are summarized in Table 7. For both parameters and across both cases, the observed dispersion is small relative to the respective actual values. The confidence intervals remain narrow and are centered close to the true parameter values, indicating minimal statistical bias in the identification process. These results demonstrate that the proposed GA–ANN framework provides consistent and repeatable parameter estimates despite the stochastic initialization of the Genetic Algorithm and the presence of noise in the pressure data.

**Table 7.** Mean estimates and 95% confidence intervals of the predicted parameters over 30 independent runs.

| | Parameters | Actual Values | Prediction over 30 Runs | | | |
|---|---|---|---|---|---|---|
| | | | Mean | Standard Deviation | Lower Bound | Upper Bound |
| Case: 1 | $\mu$ | 1 | 1.0022 | 0.0137 | 0.997 | 1.0073 |
| | $\overline{C}_1$ | 0.135 | 0.1367 | 0.012 | 0.1321 | 0.1412 |
| Case: 2 | $\mu$ | 100 | 100.67 | 0.84 | 100.36 | 100.99 |
| | $\overline{C}_1$ | 0.1 | 0.1056 | 0.0078 | 0.1027 | 0.1086 |

## 6. Conclusions

This work presented an efficient inverse identification framework for determining Mooney–Rivlin material parameters of soft membranes from pressure–volume data of the bulge test. A surrogate model based on an Artificial Neural Network was trained using data generated from FE simulations and subsequently coupled with a GA for parameter identification. The trained ANN accurately captured the nonlinear pressure–volume response of the membrane and served as a rapid substitute for the computationally expensive FE solver during optimization. As a result, the proposed approach enabled forward evaluations that were around five orders of magnitude faster than FE simulations, making the framework particularly attractive for inverse problems that require a large number of forward evaluations.

The accuracy and robustness of the method were examined using both noise-free and noisy datasets. To emulate experimental uncertainty, random noise was introduced into the pressure data. Even under these conditions, the proposed framework was able to recover the material parameters with good accuracy. In addition, multiple independent optimization runs with different noise realizations produced narrow confidence intervals around the true parameter values, demonstrating the stability, repeatability, and reliability of the identification process.

Overall, the proposed GA–ANN hybrid framework provides a computationally efficient and reliable strategy for calibrating hyperelastic material parameters from bulge test data. The proposed framework has potential applications in the mechanical characterization of soft materials used in areas such as soft robotics, biomedical devices, and flexible electronics. The methodology is sufficiently general to be extended to other hyperelastic constitutive models, including those involving a larger number of material parameters. In such cases, the overall GA–ANN framework remains unchanged; however, the higher-dimensional parameter space would generally require a larger FE-generated training dataset and increased offline computational effort for surrogate training to accurately capture the constitutive response. Once trained, the ANN surrogate can still provide rapid predictions, enabling efficient inverse identification. The same framework can also be adapted to identify additional constitutive parameters, such as those associated with surface elasticity, thereby further expanding its applicability to the characterization of soft materials. The present study is limited to validation using FE-generated datasets under controlled numerical conditions, and therefore experimental validation remains necessary to fully establish the practical applicability of the proposed methodology. Future work will focus on validating the proposed framework using experimentally measured bulge test data to establish its practical applicability. In addition, a systematic comparison of the proposed framework with deterministic optimization methods, such as gradient-based and pattern-search algorithms, represents another important direction for future research.

**Author Contributions:** Conceptualization, funding acquisition, M.R.Z.; methodology, supervision, project administration, and resources, M.R.Z., A.H.K.; software, validation, and formal analysis, S.H., S.S., and A.K.; Investigation and data curation, T.S.G.; writing—original draft preparation, all the authors; writing and visualization—all the authors. All authors have read and agreed to the published version of the manuscript.

**Funding:** M.R.Z. acknowledges the Anusandhan National Research Foundation (ANRF), Government of India, for financial support through the Core Research Grant (CRG/2023/000080), which made this work possible.

**Data Availability Statement:** The original contributions presented in this study are included in the article. Further inquiries can be directed to the corresponding authors.

**Conflicts of Interest:** The authors declare no conflicts of interest.

## References

1. Wang, W.; Narain, R.; Zeng, H. Hydrogels. In *Polymer Science and Nanotechnology*; Elsevier: Amsterdam, The Netherlands, 2020; pp. 203–244. [CrossRef]
2. Wang, C.; Wang, C.; Huang, Z.; Xu, S. Materials and Structures toward Soft Electronics. *Adv. Mater.* **2018**, *30*, 1801368. [CrossRef] [PubMed]
3. Jang, S.H.; Na, S.H.; Park, Y.L. Magnetically Assisted Bilayer Composites for Soft Bending Actuators. *Materials* **2017**, *10*, 646. [CrossRef] [PubMed]
4. Yazdi, M.K.; Vatanpour, V.; Taghizadeh, A.; Taghizadeh, M.; Ganjali, M.R.; Munir, M.T.; Habibzadeh, S.; Saeb, M.R.; Ghaedi, M. Hydrogel membranes: A review. *Mater. Sci. Eng. C* **2020**, *114*, 111023. [CrossRef] [PubMed]
5. Kang, B.B.; Lee, H.; In, H.; Jeong, U.; Chung, J.; Cho, K.J. Development of a polymer-based tendon-driven wearable robotic hand. In Proceedings of the 2016 IEEE International Conference on Robotics and Automation (ICRA), Stockholm, Sweden, 16–21 May 2016; pp. 3750–3755. [CrossRef]
6. Colas, A.; Curtis, J. Silicones. In *Handbook of Polymer Applications in Medicine and Medical Devices*; Elsevier: Amsterdam, The Netherlands, 2013; pp. 131–143. [CrossRef]
7. Nauta, A.; Larson, B.; Longaker, M.T.; Peter Lorenz, H. Scarless wound healing. In *Principles of Regenerative Medicine*; Elsevier: Amsterdam, The Netherlands, 2011; pp. 103–127. [CrossRef]

8. Wong, C.; Tummala, R. Polymers for electronic packaging in the 21st century. In *Applied Polymer Science: 21st Century*; Elsevier: Amsterdam, The Netherlands, 2000; pp. 659–676. [CrossRef]
9. Treloar, L.R.G. *The Physics of Rubber Elasticity*, 3rd ed.; Oxford University Press: Oxford, UK, 1975.
10. Luo, H.; Zhu, Y.; Zhao, H.; Ma, L.; Zhang, J. Simulation Analysis of Equibiaxial Tension Tests for Rubber-like Materials. *Polymers* **2023**, *15*, 3561. [CrossRef] [PubMed]
11. Pelliciari, M.; Sirotti, S.; Aloisio, A.; Tarantino, A.M. Analytical, numerical and experimental study of the finite inflation of circular membranes. *Int. J. Mech. Sci.* **2022**, *226*, 107383. [CrossRef]
12. Di Matteo, A.; Nuzzo, G.; Pinnola, F.P. Nonlinear response of circular hyperelastic dielectric membranes subject to inflation. *Int. J.-Non-Linear Mech.* **2026**, *181*, 105288. [CrossRef]
13. Chaudhuri, A.; DasGupta, A. On the static and dynamic analysis of inflated hyperelastic circular membranes. *J. Mech. Phys. Solids* **2014**, *64*, 302–315. [CrossRef]
14. Li, Y.; Nemes, J.A.; Derdouri, A.A. Membrane inflation of polymeric materials: Experiments and finite element simulations. *Polym. Eng. Sci.* **2001**, *41*, 1399–1412. [CrossRef]
15. Patil, A.; DasGupta, A. Finite inflation of an initially stretched hyperelastic circular membrane. *Eur. J. Mech.-A/Solids* **2013**, *41*, 28–36. [CrossRef]
16. Verron, E.; Marckmann, G.; Peseux, B. Dynamic inflation of non-linear elastic and viscoelastic rubber-like membranes. *Int. J. Numer. Methods Eng.* **2001**, *50*, 1233–1251. [CrossRef]
17. Chen, Z.; Zhu, L.; Zhan, L.; Xiao, R. Inflation of a Circular Hyperelastic Membrane: A Numerical Analysis. *Acta Mech. Solida Sin.* **2025**, *38*, 651–663. [CrossRef]
18. Selvadurai, A. Deflections of a rubber membrane. *J. Mech. Phys. Solids* **2006**, *54*, 1093–1119. [CrossRef]
19. Holzapfel, G.A.; Ogden, R.W. Modeling the biomechanical properties of soft biological tissues: Constitutive theories. *Eur. J. Mech.-A/Solids* **2025**, *112*, 105634. [CrossRef]
20. Wu, B.; Huang, C.; Li, N.; Lu, Y.; Yi, Y.; Yan, B.; Jiang, D. Formulation of Hyperelastic Constitutive Model for Human Periodontal Ligament Based on Fiber Volume Fraction. *Materials* **2025**, *18*, 705. [CrossRef] [PubMed]
21. Anssari-Benam, A.; Saccomandi, G. Continuous Softening as a State of Hyperelasticity: Examples of Application to the Softening Behavior of the Brain Tissue. *J. Biomech. Eng.* **2024**, *146*, 091009. [CrossRef] [PubMed]
22. Sirotti, S.; Pelliciari, M.; Aloisio, A.; Tarantino, A.M. A strain energy function for the inflation of hyperelastic membranes. *Mech. Mater.* **2025**, *209*, 105442. [CrossRef]
23. Destrade, M.; Saccomandi, G.; Sgura, I. Methodical fitting for mathematical models of rubber-like materials. *Proc. R. Soc. A Math. Phys. Eng. Sci.* **2017**, *473*, 20160811. [CrossRef]
24. Sheng, J.Y.; Zhang, L.Y.; Li, B.; Wang, G.F.; Feng, X.Q. Bulge test method for measuring the hyperelastic parameters of soft membranes. *Acta Mech.* **2017**, *228*, 4187–4197. [CrossRef]
25. Avril, S.; Bonnet, M.; Bretelle, A.-S.; Grédiac, M.; Hild, F.; Ienny, P.; Latourte, F.; Lemosse, D.; Pagano, S.; Pagnacco, E.; et al. Overview of identification methods of mechanical parameters based on full-field measurements. *Exp. Mech.* **2008**, *48*, 381–402. [CrossRef]
26. Hamim, S.U.; Singh, R.P. Proper Orthogonal Decomposition–Radial Basis Function Surrogate Model-Based Inverse Analysis for Identifying Nonlinear Burgers Model Parameters From Nanoindentation Data. *J. Eng. Mater. Technol.* **2017**, *139*, 041010. [CrossRef]
27. Couckuyt, I.; Aernouts, J.; Deschrijver, D.; De Turck, F.; Dhaene, T. Identification of quasi-optimal regions in the design space using surrogate modeling. *Eng. Comput.* **2013**, *29*, 127–138. [CrossRef]
28. Halloran, J.P.; Erdemir, A. Adaptive Surrogate Modeling for Expedited Estimation of Nonlinear Tissue Properties Through Inverse Finite Element Analysis. *Ann. Biomed. Eng.* **2011**, *39*, 2388–2397. [CrossRef] [PubMed]
29. Raissi, M.; Perdikaris, P.; Karniadakis, G. Physics-informed neural networks: A deep learning framework for solving forward and inverse problems involving nonlinear partial differential equations. *J. Comput. Phys.* **2019**, *378*, 686–707. [CrossRef]
30. Karniadakis, G.E.; Kevrekidis, I.G.; Lu, L.; Perdikaris, P.; Wang, S.; Yang, L. Physics-informed machine learning. *Nat. Rev. Phys.* **2021**, *3*, 422–440. [CrossRef]
31. Holzapfel, G. *Nonlinear Solid Mechanics: A Continuum Approach for Engineering*; Wiley: Hoboken, NJ, USA, 2000.
32. Ogden, R.W. *Non-Linear Elastic Deformations*; Dover Publications: Garden City, NY, USA, 1997.
33. Selvadurai, A.P.S. Mechanics of pressurized planar hyperelastic membranes. *Philos. Trans. R. Soc. A Math. Phys. Eng. Sci.* **2022**, *380*, 20210319. [CrossRef] [PubMed]